Exp Fluids (2013) 54:1576
DOI 10.1007/s00348-013-1576-5

RESEARCH ARTICLE

Wetting state and maximum spreading factor of microdroplets impacting on superhydrophobic textured surfaces with anisotropic arrays of pillars

Dae Hee Kwon · Hyung Kyu Huh · Sang Joon Lee

Received: 30 April 2013 / Accepted: 1 July 2013 / Published online: 10 July 2013

Abstract The dynamic behaviors of microdroplets that impact on textured surfaces with various patterns of microscale pillars are experimentally investigated in this study. A piezoelectric inkjet is used to generate the microdroplets that have a diameter of less than 46 μm and a controlled Weber number. The impact and spreading dynamics of an individual droplet are captured by using a high-speed imaging system. The anisotropic and directional wettability and the wetting states on the textured surfaces with anisotropically arranged pillars are revealed for the first time in this study. The impalement transition from the Cassie–Baxter state to the partially impaled state is evaluated by balancing the wetting pressure P_{wet} and the capillary pressure P_C even on the anisotropic textured surfaces. The maximum spreading factor is measured and compared with the theoretical prediction to elucidate the wettability of the textured surfaces. For a given Weber number, the maximum spreading factor decreases as the texture area fraction of the textured surface decreases. In addition, the maximum spreading factors along the direction of longer inter-pillar spacing always have smaller values than those along the direction of shorter inter-pillar spacing when a droplet impacts on the anisotropic arrays of pillars.

1 Introduction

The water repellency of a textured surface is closely related to the wetting state of droplets because droplets in the Cassie–Baxter state (Cassie and Baxter 1944) have higher contact angle (CA) and lower CA hysteresis compared with those in the Wenzel state (Lafuma and Quere 2003; Wenzel 1936). The Cassie–Baxter state is often metastable (He et al. 2004; Reyssat et al. 2008), and the impalement transition to the Wenzel state may occur because of external stimuli such as abrupt pressure and the impact of droplets (Bartolo et al. 2006; Moulinet and Bartolo 2007). In addition, the transition to the Cassie impregnating state can occur under vibration of droplets (Bormashenko et al. 2008, 2012). Given that numerous practical applications of water-repellent surfaces accompany the impact process of droplets, the wetting states of droplets impacting on a textured surface are of interest.

On a surface with isotropic arrangement of pillars, the detailed impact behaviors (e.g., bouncing or non-bouncing behaviors) as well as the wetting states of impacting droplets are well understood. The wetting state of an impacting droplet depends on the balance between the wetting pressure (P_{wet}) and the antiwetting pressure ($P_{antiwet}$) (Bartolo et al. 2006; Reyssat et al. 2006). The P_{wet} of an impacting droplet consists of the dynamic pressure (P_D) and the water hammer pressure (P_{WH}). In the initial contact instant, the contact between the impacting droplet and the textured surface induces the water hammer pressure (Engel 1955; Field 1999). At the spreading stage after the contact phase, the wetting pressure is decreased to the dynamic pressure (Deng et al. 2009). The $P_{antiwet}$ that impedes the impalement transition is the capillary pressure (P_C) of the textured surface (Jung and Bhushan 2008; Kwon et al. 2011).

Given that the high value of P_{WH} falls to the value of P_D as the droplet enters the spreading stage (i.e., $P_{WH} > P_D$), three different wetting states are possible: the Cassie–Baxter state ($P_C > P_{WH} > P_D$), the Wenzel state ($P_{WH} > P_D > P_C$), and the partially impaled state

D. H. Kwon · H. K. Huh · S. J. Lee (✉)
Department of Mechanical Engineering, Center for Biofluid and Biomimic Research, POSTECH, San 31, Hyoja-dong, Pohang 790-784, Republic of Korea
e-mail: sjlee@postech.ac.kr

($P_{WH} > P_C > P_D$) (Deng et al. 2009). As an index to describe the transition between bouncing and non-bouncing behaviors, the Weber number (We) defined as $We = \rho V^2 D_0/\gamma$ can be used, where ρ is the density, V is the terminal velocity, D_0 is the initial diameter before the impact, and γ is the interfacial tension of the droplet (Kwon and Lee 2012). Based on the values of P_{wet}, $P_{antiwet}$, and We, the wetting states and detailed behaviors of the droplet after impact on the surface with an isotropic array of pillars are schematically shown in Fig. 1. However, the impact behaviors and wetting states on the textured surfaces with anisotropically patterned pillars have not been experimentally verified to date.

For anisotropic wettability that results from the anisotropic geometry of a surface, the CA of sessile droplets on the surfaces with parallel grooves were experimentally investigated (Zhao et al. 2007; Xia and Brueck 2008). In case of focusing our interest on impacting droplet due to its significance in practical applications, the surfaces with microgrooves and pillars have been studied. In studies on both types of surfaces, the maximum spreading factor has been employed to understand the basic physics behind impact dynamics. The maximum spreading factor is defined as the ratio of the maximum spreading diameter (D_m) to the initial diameter before the impact (D_0). On surfaces that comprise parallel grooves, the motion of the triple-phase contact line is suppressed. Therefore, the maximum spreading factor ($\beta_{max} = D_m/D_0$) on the grooved surface is smaller than that on the corresponding smooth surface. However, no major differences were observed between the β_{max} measured along the groove direction and perpendicular to the groove direction (Kannan and Sivakumar 2008; Vaikuntanathan et al. 2010).

For pillar-type textured surfaces, the β_{max} is revealed to be affected by the geometrical parameters of the pillar array and by the wetting state of the impacting droplet. Considering these parameters and wetting states (e.g., the Cassie–Baxter or Wenzel states), some prediction models for the maximum spreading factor (β_{max}) have been suggested (Lee and Lee 2011; Li et al. 2013). Anisotropic wetting behaviors, such as the rhombus spreading pattern, were found even though the arrangement of pillars is isotropic (Li et al. 2013; Sivakumar et al. 2005). However, anisotropic wettability with certain directionality has not been reported on the textured surface with isotropically arranged pillars.

At this point, the study on the water repellency and the anisotropic wettability arising from the textured surface with anisotropic arrangement of pillars is essential and timely. In the case of droplet impact, water repellency depends on the wetting states, and anisotropic wettability can be evaluated via β_{max}. Therefore, the wetting states and the β_{max} of impacting droplets on the surface with an anisotropic array of pillars are experimentally investigated in this study. The diameter of the impacting droplet is restricted to less than 50 μm to exclude the gravitational effect. In addition, the impact dynamics are discussed in terms of the interaction between the inertia, surface, and viscous effects.

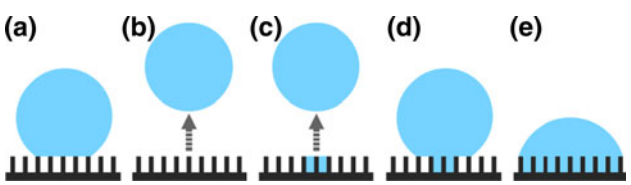

Fig. 1 Schematic wetting states of impacting droplets after impact on a textured surface. **a** Non-bouncing (NB) in the Cassie–Baxter state, **b** bouncing (B) in the Cassie–Baxter state, **c** bouncing with part of liquid partially penetrated into interstices (PPB), **d** second non-bouncing (2NB) in the partially impaled state, and **e** Wenzel or sticky (S) state

2 Experimental setup

A schematic diagram of the experimental setup utilized in this study is depicted in Fig. 2. The inkjet printing system, textured surfaces, and optical apparatus are placed on a vibration isolation table to prevent external disturbances. In addition, the experimental setup is covered by an acrylic shield to maintain temperature and humidity conditions.

Microscale droplets are generated from a piezoelectric inkjet printhead (MJ-AT-050, MicroFab Technologies Inc.). Deionized water filtrated through a GE nylon syringe filter with 5 μm pores is inkjet printed with controlled initial diameter D_0 and terminal velocity V. This control is

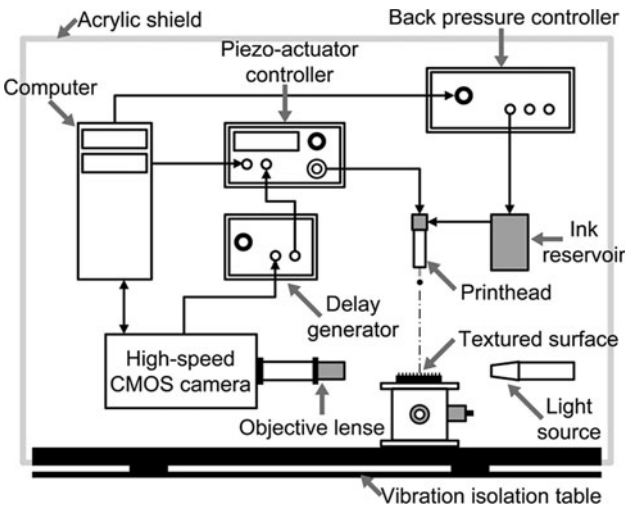

Fig. 2 Schematic diagram of the experimental setup

accomplished by varying the waveform of the applied voltage to the piezo-actuator of the inkjet printhead.

According to the D_0 and V of the microdroplets, several key parameters which describe the impact phenomenon are determined. The parameters include the Reynolds number (Re), the Ohnesorge number (Oh), the Bond number (Bo), and the previously mentioned Weber number (We). These dimensionless groups are defined as $Re = \rho V D_0/\mu$, $Oh = \sqrt{We}/Re$, and $Bo = \rho g D_0^2/\gamma$, where μ is the viscosity of the droplet and g is the acceleration of gravity.

For the impact of microdroplets on a textured surface, the following two wetting pressures, P_D and P_{WH}, are significant:

$$P_D = 0.5\rho V^2 \quad (1)$$

$$P_{WH} = 0.003\rho CV \quad (2)$$

where C is the sound speed of the droplet (Kwon and Lee 2012). The ranges of the experimental parameters of the impacting droplets in this study are summarized in Table 1.

The textured surfaces of photoresist (SU-8, MicroChem Corp.) are fabricated by using standard photolithography followed by coating of (tridecafluoro-1,1,2,2-tetrahydrooctyl) trichlorosilane (Sigma-Aldrich Co.) through vapor phase deposition. The cylindrical pillars on the surfaces have identical diameters ($d = 3.2$ μm) and heights ($H = 20$ μm) throughout the entire surface. Four different patterns of the same pillars are arrayed on each surface, as shown in Fig. 3. The textured surfaces with an isotropic array of pillars are denoted as T_S, where subscript S indicates inter-pillar spacing. For an anisotropic array of pillars, the subscript $S_A \perp S_B$ is used to represent inter-pillar spacings along two perpendicular directions, as indicated in Fig. 3c. The two isotropic arrays ($T_{2.8}$ and $T_{5.8}$, respectively) are prepared for comparison and to accentuate the effect of the anisotropic pillar arrays of $T_{2.8\perp5.8}$ and $T_{2.8\perp8.8}$.

The mechanism of the impalement transition should be considered when evaluating the value of P_C of the textured surface. Two possible mechanisms exist: the sag mechanism

Table 1 Experimental parameters of impacting droplets tested in this study

Parameters studied	D_0 (μm)	V (m/s)	Bo ($\times10^{-4}$)	We	Re	Oh ($\times10^{-2}$)	P_D (kPa)	P_{WH} (kPa)
Min.	40.3	1.12	2.32	0.84	78.7	1.14	0.62	5.00
Max.	45.9	2.38	3.16	3.33	154	1.24	2.82	10.6

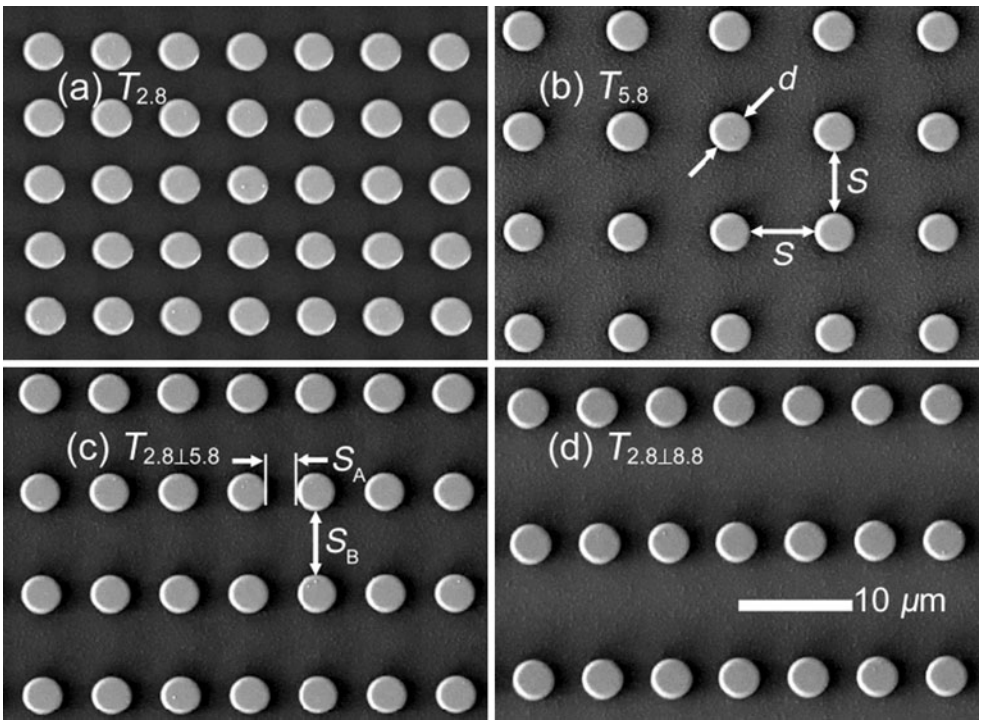

Fig. 3 SEM images (*top view*) of the textured surfaces that have isotropic arrays of pillars with inter-pillar spacing (S) of **a** 2.8 μm ($T_{2.8}$) and **b** 5.8 μm ($T_{5.8}$), and having anisotropic arrays with $S_A = 2.8$ μm, and **c** $S_B = 5.8$ ($T_{2.8\perp5.8}$) and **d** $S_B = 8.8$ μm ($T_{2.8\perp8.8}$)

and the de-pinning mechanism. In the sag mechanism, the air–liquid interface pinned on the top of the texturing features touches the basal surface (Fig. 4a). If the CA exceeds the local advancing CA (θ_A), the pinned contact line detaches from the top of the texturing features and slides downward to touch the basal surface (Fig. 4b). The values of P_C based on the de-pinning mechanism ($P_{C,depin}$) are calculated as (Kwon et al. 2011)

$$P_{C,depin} = -\frac{\pi d\gamma \cos\theta_A}{(S_A + d)(S_B + d) - \pi d^2/4} \quad (3)$$

The value of θ_A measured on the smooth surface is approximately 114°. The calculated $P_{C,depin}$ for the textured surfaces used in this study are presented in Table 2. The analytic solution from the balance of force on the air–liquid interface is available to calculate the values of P_C based on the sag mechanism ($P_{C,sag}$) (Zheng et al. 2005). Furthermore, the $P_{C,sag}$ of the textured surfaces with randomly distributed circular pillars can be predicted based on the work of Emami et al. (2011). However, the textured surfaces used in this study are made such that the sag transition cannot occur by sufficiently increasing the height of pillars (Kwon et al. 2011; Kwon and Lee 2012). Therefore, the impacting droplets with P_{wet} greater than $P_{C,depin}$ will undergo impalement transition via the de-pinning mechanism. In other words, the $P_{antiwet}$ of the textured surfaces prepared in this experiment is the corresponding value based on de-pinning mechanism $P_{C,depin}$.

In discussing the wetting states of the textured surfaces, the texture area fraction (ϕ) and roughness factor (ζ) are incorporated as major parameters. Both parameters indicate the area ratio of solid surface in contact with water to the projected area. In the Cassie–Baxter state, the ratio is denoted as ϕ, whereas ζ represents the ratio in the Wenzel state. These ratios are presented in Table 2 and defined as (Bartolo et al. 2006)

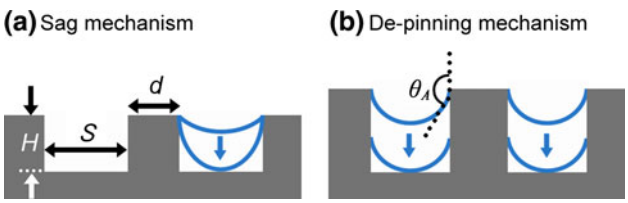

Fig. 4 Schematics (*side view*) of the two impalement transition mechanisms

$$\phi = \frac{\pi d^2/4}{(S_A + d)(S_B + d)} \quad (4)$$

$$\varsigma = \frac{(S_A + d)(S_B + d) + \pi dH}{(S_A + d)(S_B + d)} \quad (5)$$

Images of the impacting microscale droplets are captured at a frame rate of 2.5×10^5 (4 μs time interval between consecutive frames) by using a high-speed camera (FASTCAM SA 1.1, Photron Inc.) with an exposure time of 1 μs. The objective lens has a numerical aperture of 0.35 and magnification of 20. To observe the anisotropic behaviors on the textured surfaces having anisotropic arrays, the impacting droplets are imaged at two perpendicular directions parallel to S_A and S_B. The two imaging directions parallel to S_A and S_B are denoted as $\|S_A$ and $\|S_B$, respectively. For an impact event, simultaneous imaging at two orthogonal directions is practically difficult to achieve. Therefore, an imaging at each imaging direction ($\|S_A$ or $\|S_B$) is conducted separately. The impact conditions, including the velocity and diameter of a droplet, are maintained identical for a set of imaging at both directions.

The captured grayscale images are converted to binary images to digitally process the morphological information of droplets. Each droplet is recognized and processed as a set of pixels. In this optical setup, one pixel in an image is approximately 1.12×1.12 μm^2 in physical dimension. The exposure time of 1 μs is sufficient to resolve the dynamic motion of an impacting droplet, and no blur is observed. Therefore, the measurement error mainly depends on the precision in detecting the droplet boundary. For all images obtained in this study, the threshold levels used in the conversion to binary images are examined and adjusted to minimize the measurement error.

3 Results and discussion

3.1 Impact phenomenology

The parameter space of *Re* and *We* of the impacting microdroplets in this study is plotted in Fig. 5. The range of these parameters indicates that the impact and spreading dynamics are governed by the balance between the inertia

Table 2 Topographic and water-repellent properties of the textured surfaces used in this study

Surface	Pillar array	d (μm)	H (μm)	S_A (μm)	S_B (μm)	ϕ	ζ	$P_{C,depin}$ (kPa)	θ_{CB} (°)
$T_{2.8}$	Isotropic	3.2	20	2.8		0.223	6.58	9.98	150.2
$T_{5.8}$		3.2	20	5.8		0.099	3.48	3.83	160.2
$T_{2.8\perp5.8}$	Anisotropic	3.2	20	2.8	5.8	0.149	4.72	6.07	155.7
$T_{2.8\perp8.8}$		3.2	20	2.8	8.8	0.112	3.79	4.36	159.0

and the capillary effect, based on the work of Schiaffino and Sonin (1997). From their perspective, the viscous effect is negligible for the impact regime of our study.

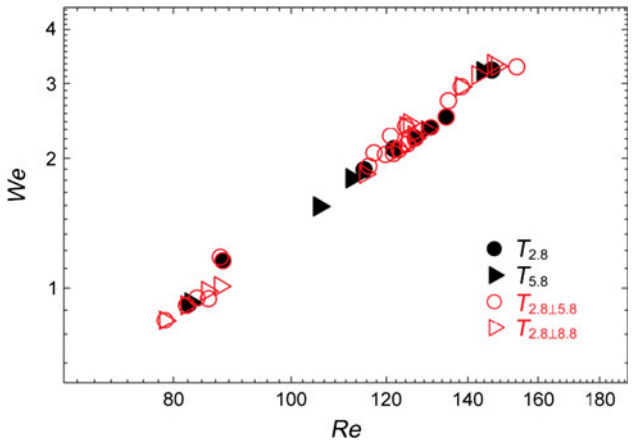

Fig. 5 Parameter space of Reynolds and Weber numbers for this study

Clanet et al. (2004) proposed the impact number $I = We/Re^{4/5}$ as another standpoint of the impact regime. For $I < 1$, the impact is dominated by the capillary force, and the inviscid impact regime is expected. Given that the values I of the microdroplets tested in this study are smaller than 0.08, the viscous effect is also negligible from this standpoint. The gravitational effect is obviously uninfluential as indicated by small values of Bo (Table 1).

In this impact regime, the microdroplets spread on the textured surfaces gently, and no splashing is observed, as shown in Figs. 6 and 7. This finding is consistent with the experimental results of the impacting microdroplets on smooth surfaces, and the splashing was considered restrained by the strong surface tension caused by small-scale droplets (Son et al. 2008; van Dam and Le Clerc 2004; Visser et al. 2012). The shapes of the spreading microdroplets are not subdivided into the rim and lamella. Instead, the microdroplets deform into a pancake shape with rounded sides at the maximum spread as a result of the small We values in this study. It was shown that the

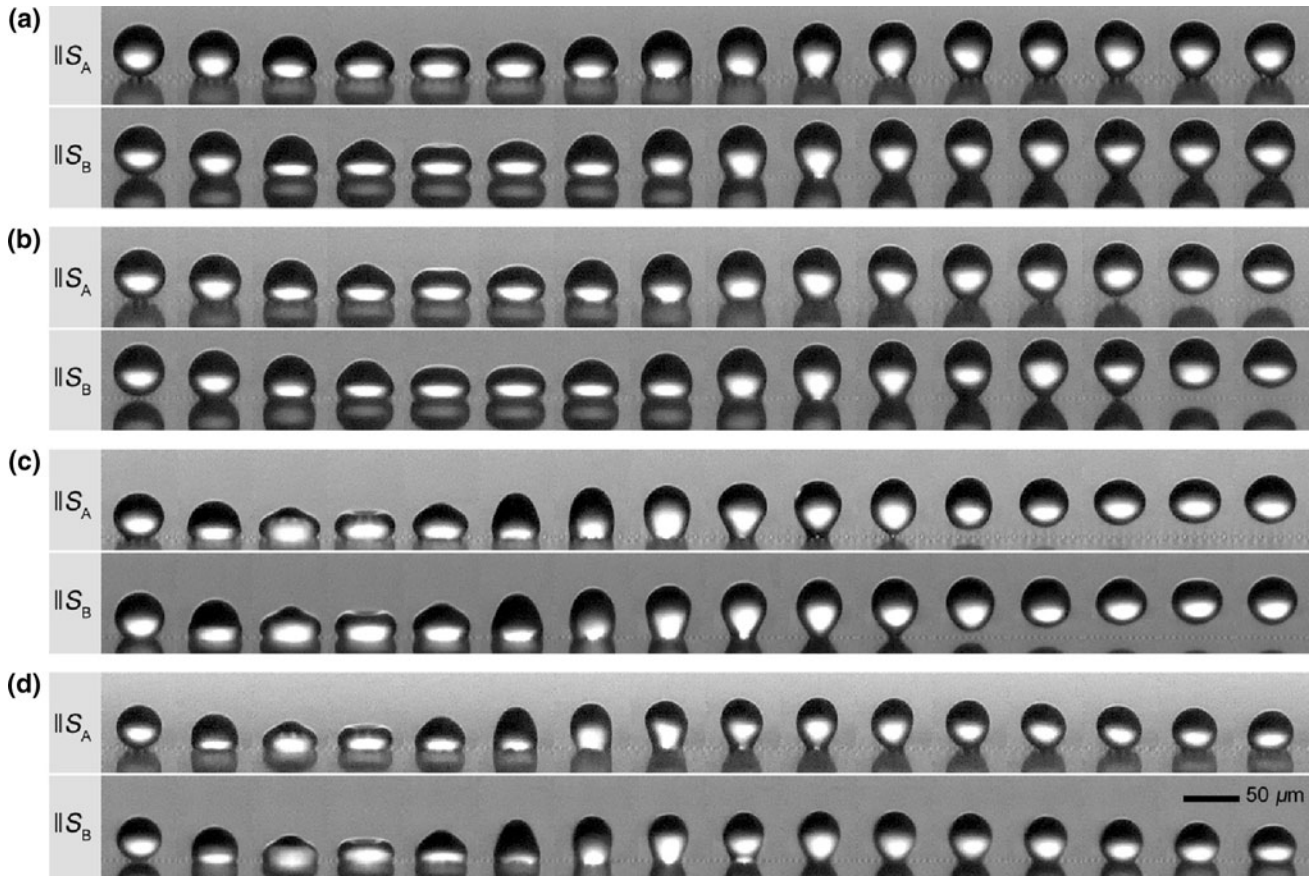

Fig. 6 Drop impact sequences on the textured surface $T_{2.8\perp5.8}$ recorded separately in two perpendicular directions, $\|S_A$ and $\|S_B$. The time interval between consecutive images is 4 μs. The impact conditions of droplets are **a** $D_0 = 45.9$ μm, $V = 1.12$ m/s, $We = 0.84$, $P_D = 0.62$ kPa, $P_{WH} = 5.0$ kPa, **b** $D_0 = 45.9$ μm, $V = 1.19$ m/s, $We = 0.95$, $P_D = 0.70$ kPa, $P_{WH} = 5.32$ kPa, **c** $D_0 = 43.7$ μm, $V = 1.79$ m/s, $We = 2.04$, $P_D = 1.60$ kPa, $P_{WH} = 8.0$ kPa, and **d** $D_0 = 40.3$ μm, $V = 1.96$ m/s, $We = 2.26$, $P_D = 1.91$ kPa, $P_{WH} = 8.76$ kPa

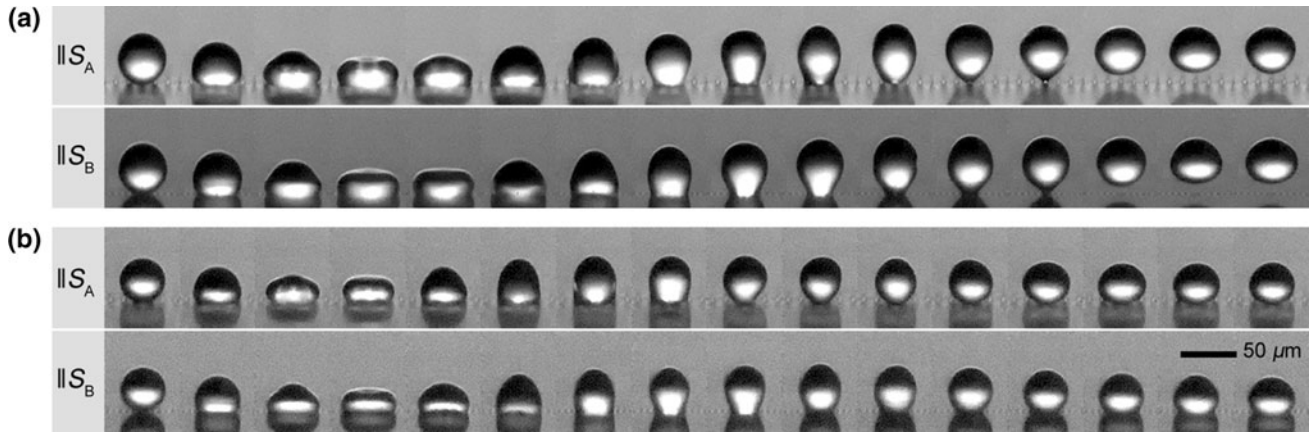

Fig. 7 Drop impact sequences on the textured surface $T_{2.8\perp 8.8}$ recorded separately in two perpendicular directions, $\|S_A$ and $\|S_B$. The time interval between consecutive images is 4 μs. The impact conditions of droplets are **a** $D_0 = 44.8$ μm, $V = 1.82$ m/s, $We = 2.16$, $P_D = 1.65$ kPa, $P_{WH} = 8.13$ kPa, and **b** $D_0 = 40.3$ μm, $V = 2.03$ m/s, $We = 2.42$, $P_D = 2.05$ kPa, $P_{WH} = 9.07$ kPa

presence of the rim and lamella structures depended on the *We* even for microdroplets (van Dam and Le Clerc 2004).

After the maximum spread, the contact line recedes and the microdroplet shows different dynamic behaviors according to its wetting state and *We* value. However, the difference in the impact sequence between the two imaging directions is not so significant in terms of phenomenology.

3.2 Wetting states and impact behaviors

On the textured surface $T_{2.8\perp 5.8}$, the microdroplets with values of P_{wet} (P_D and P_{WH}) smaller than P_C ($P_{C,depin} = 6.07$ kPa) exhibit non-bouncing (NB) and bouncing (B) behaviors, as depicted in Fig. 6a, b, respectively. In this pressure range ($P_C > P_{WH} > P_D$), the *We* values of the B droplets are always higher than those of the NB droplets. In addition, the microdroplets should be in the Cassie–Baxter state due to their smaller P_{wet} than the P_C. As the *We* of the microdroplets further increases, the P_{WH} exceeds the P_C and the impacting microdroplets still exhibit bouncing behavior. A typical example of these microdroplets is presented in Fig. 6c. The pressure range of this microdroplet ($P_{WH} > P_C > P_D$) implies that the impalement transition occurs, and the microdroplet is in the partially impaled state.

To verify the wetting states according to the balance between the P_{wet} and the P_C, the bouncing microdroplets in different pressure ranges (e.g., Fig. 6b, c) are compared. In our previous study (Kwon and Lee 2012), the impalement transition was verified by checking the position of the remaining liquid on the textured surface after the departure of the bouncing droplet from the surface. The remnant liquid was identified based on the difference in the grayscale intensities of the region near the textured surface in the images captured before and after impact. The wetting state was considered to be in the partially impaled state when the remnant liquid was retained in the inter-pillar space after the impact. On the contrary, the remnant liquid at the pillar top signified the Cassie–Baxter state without penetration of liquid into the inter-pillar space.

In this study, the remaining liquid of a microdroplet with $P_{wet} < P_C$ is always positioned at the top of the pillars. For the microdroplets with $P_{WH} > P_C$, the remnant liquid is observed at the inter-pillar space. The grayscale intensity variations of the bouncing droplets in Fig. 6b, c are indicated in Fig. 8. The shaded regions in the graph denote the position of the pillars. Along the imaging direction parallel to S_A, the remnant liquid of the microdroplet in Fig. 6b is positioned on the pillar top (Fig. 8a). However, for the microdroplet in Fig. 6c, the difference in the grayscale intensity at the inter-pillar spaces is relatively high (as much as 36 %). This implies that the remnant liquid also exists at the inter-pillar spaces. In the direction along $\|S_B$, the presence of the remnant liquid at the inter-pillar space for the microdroplet in Fig. 6c is identified more clearly (Fig. 8b). Therefore, the impalement transition via the depinning mechanism can be evaluated by weighing the P_{wet} and P_C even for the textured surfaces with an anisotropic array of pillars. In other words, the balance between the P_{wet} and P_C is still a valid criterion for the textured surface that has an anisotropic array of pillars to estimate the wetting states of the impacting droplets. This is attributed to the fact that the capillary pressure P_C of any impalement mechanism is deduced and calculated from a unit cell of pillars in which the pattern of the pillars is already reflected.

For the case of $P_{WH} > P_C$, however, whether the liquid touches the basal surface or not is unclear, as observed in our previous study. For this reason, the bouncing droplets

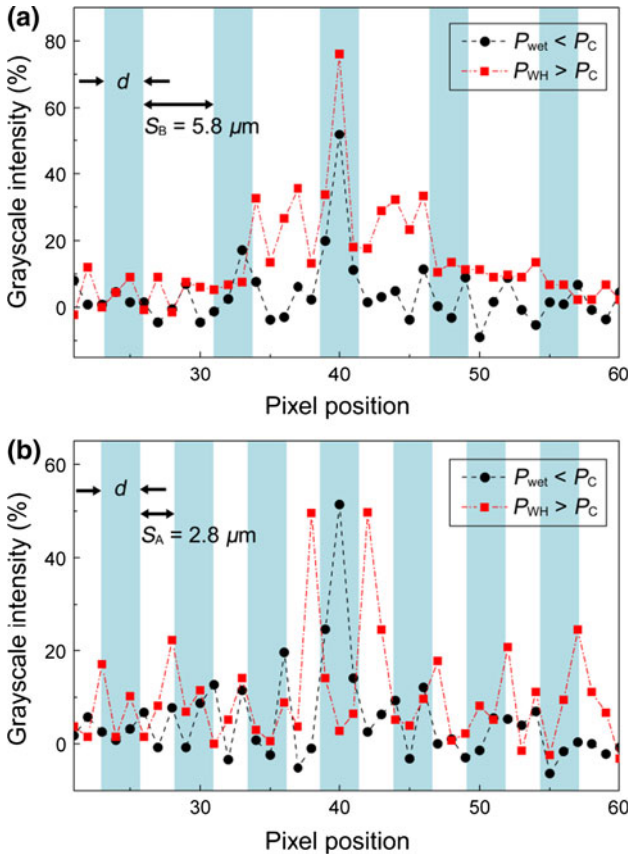

Fig. 8 Differences between the *grayscale* intensities of the textured surface regions before the impact and after the departure of microdroplets. The *grayscale* intensities are measured along the directions **a** $\|S_A$ and **b** $\|S_B$

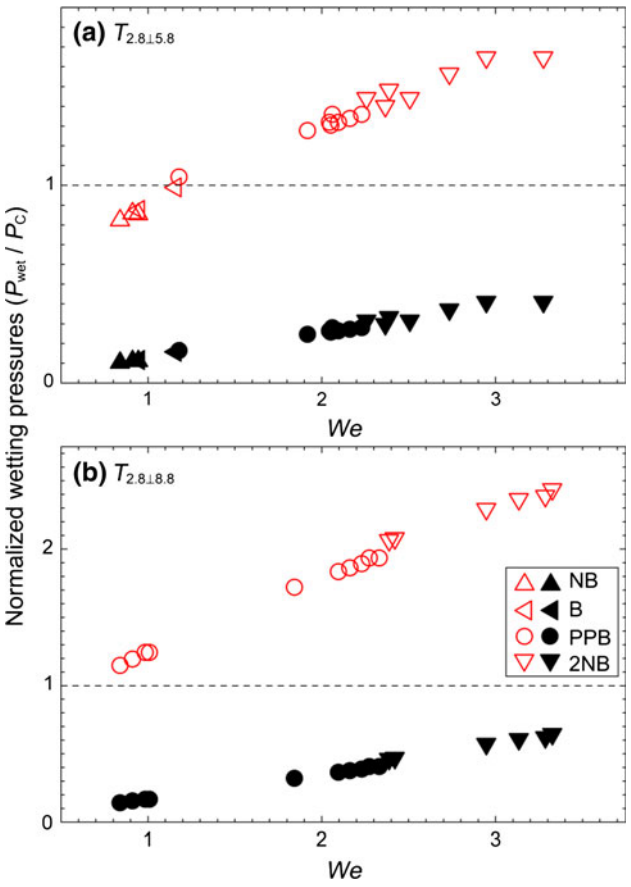

Fig. 9 Normalized wetting pressures (P_{wet}/P_C) according to the Weber number of the impacting microdroplets on **a** $T_{2.8\perp5.8}$ and **b** $T_{2.8\perp8.8}$. The normalized P_{WH} values of the microdroplets are marked with *open symbols*, whereas the normalized P_D values are marked with *solid symbols*. The wetting states are evaluated by the balance between the wetting pressure P_{wet} and the capillary pressure P_C. The impact behaviors are distinguished by the Weber number

in the pressure range of $P_{WH} > P_C > P_D$ are referred to as the partially penetrated bouncing (PPB) droplets.

In the partially impaled state ($P_{WH} > P_C > P_D$), the impacting droplets exhibit non-bouncing behavior as the values of *We* increase over a certain critical value, as shown in Figs. 6d and 7b. The *We* of these second non-bouncing (2NB) droplets are always higher than those of the PPB droplets.

The kinetic energy of the impacting droplet should be greater than the surface energy dissipated during the retraction phase in the bouncing behavior (Reyssat et al. 2006; Bartolo et al. 2006). These two energies are scaled into a dimensionless parameter, the Weber number *We*. The *We* can be used as an index to describe the transition of the impact behaviors on the textured surfaces with isotropic arrays of pillars (Kwon and Lee 2012). Even for the textured surfaces $T_{2.8\perp5.8}$ and $T_{2.8\perp8.8}$, the *We* is a suitable index to describe the transition between the bouncing and non-bouncing behaviors (NB → B and PPB → 2NB), as shown in Fig. 9.

The Cassie impregnating state hardly occurs for impacting droplets (Li et al. 2013). In the receding stage of drop impact, however, the Cassie impregnating state would be possible if the receding contact line withdraws from the mixture of the solid and liquid (Bico et al. 2002). In this study, the liquid which fills the inter-pillar space beyond the contact line of the receding droplet is not observed. As shown in Fig. 8, the liquid exists inside the inter-pillar space only in the vicinity of the initial contact point where the P_{WH} exceeds the P_C. Therefore, the Cassie impregnating state is inaccessible in this study.

3.3 Maximum spreading factor

The maximum spreading factor (β_{max}) is investigated to evaluate the anisotropic and directional wettability that arises from the anisotropic arrangement of microscale pillars. The β_{max} of the impacting microdroplets on textured surfaces are reported for the first time in this study. To elucidate the effect of anisotropic patterns of pillars, the β_{max} on the textured surfaces with isotropic arrays of pillars

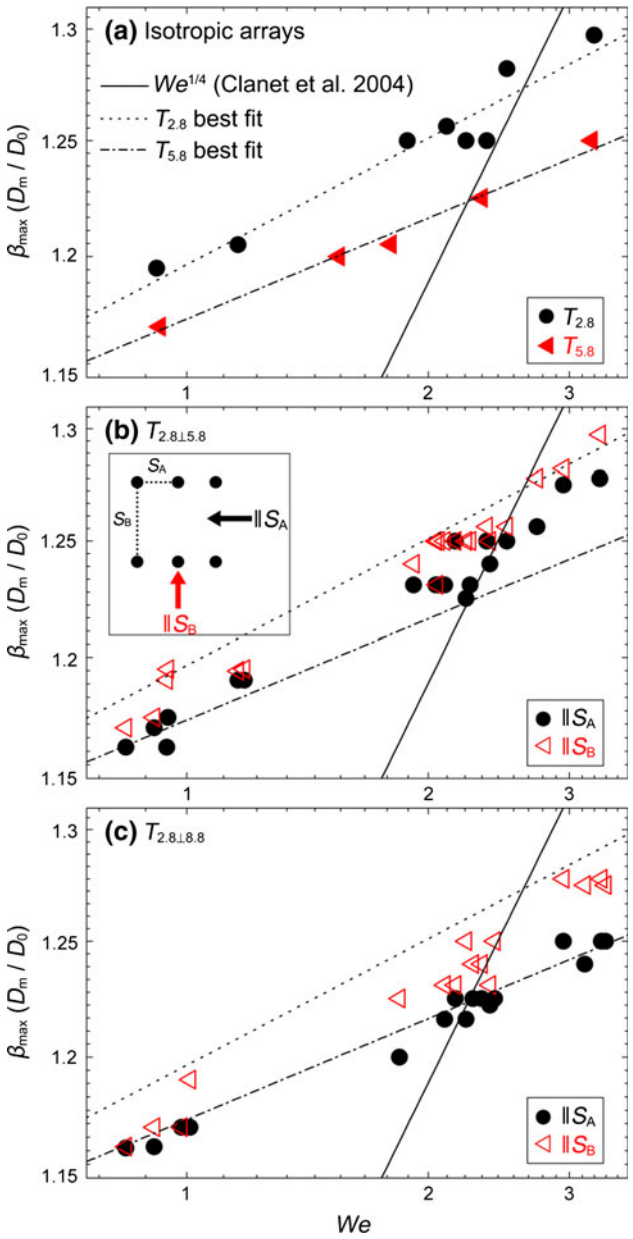

Fig. 10 Maximum spreading factors (β_{max}) of impacting microdroplets in this study. The β_{max} on **a** $T_{2.8}$ and $T_{5.8}$, **b** $T_{2.8\perp5.8}$, and **c** $T_{2.8\perp8.8}$ are shown

are also measured for comparison (Fig. 10a). As discussed previously, the small impact number of this study (I <0.08) is indicative of the capillary-driven impact regime. In the capillary regime, the β_{max} was scaled as $We^{1/4}$ (Clanet et al. 2004). However, the β_{max} are scaled as $We^{0.06}$ and $We^{0.05}$ on the textured surfaces $T_{2.8}$ and $T_{5.8}$, respectively. The exponents 0.06 and 0.05 are significantly lower than the exponent estimated in the capillary regime. This disagreement between the experimental data and the theoretical estimation was also reported in the literature in which the impacting droplets were in microscale (Visser et al. 2012). In the literature, the small exponents and the resultant low β_{max} were considered to be from the microscale where viscous effects were pronounced. The low β_{max} values in this study are also attributed to the microscale droplets although the surfaces are textured surfaces with pillars.

The geometric parameters of the textured surface clearly affect the β_{max} for a given We. On the isotropic arrays of pillars, the β_{max} on $T_{2.8}$ is larger than that on $T_{5.8}$ for a given We. As the inter-pillar spacing (S) of the textured surface increases, the texture area fraction (ϕ) decreases and the CA estimated in the Cassie–Baxter state (θ_{CB}) increases, as illustrated in Table 2. On the assumption that the hydrophobic nature of the textured surfaces is represented by the θ_{CB}, the ϕ that determines the θ_{CB} can be used to explain the β_{max} on the textured surfaces with various arrays of pillars. The lower ϕ of $T_{5.8}$ compared with that of $T_{2.8}$ results in higher θ_{CB} values, which represents higher degree of hydrophobicity. Therefore, the impacting droplets on $T_{5.8}$ encounter more resistance in spreading outward than those on $T_{2.8}$ and exhibit lower β_{max}.

On the $T_{2.8\perp5.8}$, the β_{max} measured along the two orthogonal directions $\|S_A$ and $\|S_B$ are depicted in Fig. 10b. Most of the β_{max} on the $T_{2.8\perp5.8}$ lie between those on the $T_{2.8}$ and $T_{5.8}$. This observation is consistent with the intermediate value of the ϕ (0.149) and the resulting θ_{CB} (155.7°) of the $T_{2.8\perp5.8}$ compared with those of the $T_{2.8}$ and $T_{5.8}$. In other words, the β_{max} of a textured surface is considered to be dependent on its values of the ϕ.

The value of the ϕ (0.112) on the $T_{2.8\perp8.8}$ is smaller than that of the $T_{2.8\perp5.8}$ and is still between those of the $T_{2.8}$ and $T_{5.8}$. According to the discussion of the β_{max} with respect to ϕ, the β_{max} on the $T_{2.8\perp8.8}$ is predicted to be lower than that on the $T_{2.8\perp5.8}$ and in between those on the $T_{2.8}$ and $T_{5.8}$ for a given We. As predicted from the value of the ϕ, the majority of the β_{max} on the $T_{2.8\perp8.8}$ are lower than those on the $T_{2.8\perp5.8}$ as shown in Fig. 10c. Although the β_{max} measured along $\|S_A$ approximately cover the values on the $T_{5.8}$, the overall values of the β_{max} on the $T_{2.8\perp8.8}$ lie between those of the $T_{2.8}$ and $T_{5.8}$.

For the textured surfaces with anisotropic arrays of pillars, the β_{max} measured along $\|S_B$ are definitely larger than those along $\|S_A$. In other words, the spread is restricted (enhanced) along the direction in which the inter-pillar spacing is larger (shorter). In the present impact regime, the mean differences between the β_{max} measured along the two orthogonal directions on the $T_{2.8\perp5.8}$ and $T_{2.8\perp8.8}$ are 1.02 and 1.48 %, respectively. The maximum differences are also as small as 2.04 and 2.82 % on $T_{2.8\perp5.8}$ and $T_{2.8\perp8.8}$, respectively. One reason for this weak directionality or anisotropy seems to be attributed to the small scale of the impacting droplet. The surface energy in

the microscale droplet is considered so dominant that the kinetic energy is insufficient to transform the droplet shape into the anisotropic or directional one. Also, viscous dissipation would occur inside the inter-pillar space as the *We* of the impacting microdroplet increases to the partially impaled state (Hyväluoma and Timonen 2009). From the dissipation, the impacting droplet will lose its kinetic energy which could be used as a shape deformation.

These considerations of the impact dynamics can be observed by comparing the current experimental results with the energy balance models. Before the impact, the kinetic energy (KE_1) and surface energy (SE_1) of an impacting droplet can be given by

$$KE_1 = \frac{\pi}{12}\rho V^2 D_0^3 \tag{6}$$

$$SE_1 = \pi D_0^2 \gamma \tag{7}$$

Pasandideh-Fard et al. (1996) described the surface energy at the maximum spread (SE_2) with a cylindrical droplet shape as

$$SE_2 = \frac{\pi}{4} D_m^2 \gamma (1 - \cos\theta_A) \tag{8}$$

The work done against viscosity until the maximum spread (W) was given as

$$W = \frac{\pi}{3}\rho V^2 D_0 D_m^2 \frac{1}{\sqrt{Re}} \tag{9}$$

From the energy balance equation ($KE_1 + SE_1 = SE_2 + W$), they obtained the following prediction model of the β_{max}

$$\beta_{max} = \sqrt{\frac{We + 12}{3(1 - \cos\theta_A) + 4\left(We/\sqrt{Re}\right)}} \tag{10}$$

In addition, Ukiwe and Kwok (2005) modified the SE_2 term by fully evaluating the cylindrical shape of the droplet at the maximum spread. The modified surface energy (SE_2') was expressed as

$$SE_2' = \pi\gamma \frac{2D_0^3}{3D_m} + \frac{\pi}{4}\gamma D_m^2 (1 - \cos\theta_Y) \tag{11}$$

where θ_Y is the Young contact angle. Combining Eqs. 6, 7, 9, and 11, they established the modified model given as

$$(We + 12)\beta_{max} = 8 + \beta_{max}^3 \left[3(1 - \cos\theta_Y) + 4\frac{We}{\sqrt{Re}}\right] \tag{12}$$

Recently, Li et al. (2013) established the predicting model to incorporate the effects arising from the textured surface into the theoretical model that predicts the β_{max}. They proposed the new surface energy and viscous dissipation terms. However, their model predicts negative values of the β_{max} in this impact regime, which may have resulted from an overestimation of the effects of textured surfaces in the new energy terms for the impact regime of this study.

By contrast, the model proposed by Ukiwe and Kwok (2005) demonstrates good agreement with our experimental data (Fig. 11), although this model was developed for smooth surfaces. On the smooth surfaces, Visser et al. (2012) reported that the β_{max} of microdroplets were well estimated by the model of Pasandideh-Fard et al. in which 180° was substituted for θ_A. As illustrated in Fig. 11, the prediction model (Eq. 10) with $\theta_A = 180°$ fits relatively well compared with that of $\theta_A = 114°$, which is obtained in this study. However, these two predictions overestimate the β_{max} up to 46.9 %. Substituting 180° for θ_A or θ_Y seems to lower the predicted β_{max} values.

It is interesting to note that the relative mean error of the Ukiwe and Kwok model (Eq. 12) with respect to our experimental data is only 4.11 %, whereas the relative mean error relative to their own experimental data was 5.09 %. As emphasized by Ukiwe and Kwok (2005), the CA terms in the model come from the Young equation to simplify the SE_2. The equilibrium CA of this study (110°) is used as θ_Y. Therefore, the full evaluation of the cylindrical shape as provided in Eq. 11 and the use of the equilibrium CA may have led to the significant agreement with our experimental data.

For all the surfaces tested in this study, the difference between the Ukiwe and Kwok model and experimental data increases as the *We* increases. This finding is consistent with the fact that the wetting states of microdroplets become the partially impaled state as the *We* increases, as shown in Fig. 11. In addition, the impaled volume and the resulting viscous dissipation increase as the *We* increases (Hyväluoma and Timonen 2009). Given that the model was established based on smooth surfaces, the difference between the theoretical model and our experimental data on the textured surfaces is natural. Therefore, further modification of the model is required to incorporate the dissipation at the inter-pillar space for the partially impaled state. However, the motion of the triple-phase contact line on the pillars has to be estimated prior to the modification. To the best of our knowledge, such estimation is only possible through numerical studies and is beyond the scope of this study.

4 Conclusion

In this study, the wetting states and anisotropic spreading characteristics are experimentally studied on textured surfaces having anisotropic arrays of pillars. The wetting states of the impacting microdroplets are evaluated by balancing the wetting pressure P_{wet} and the capillary

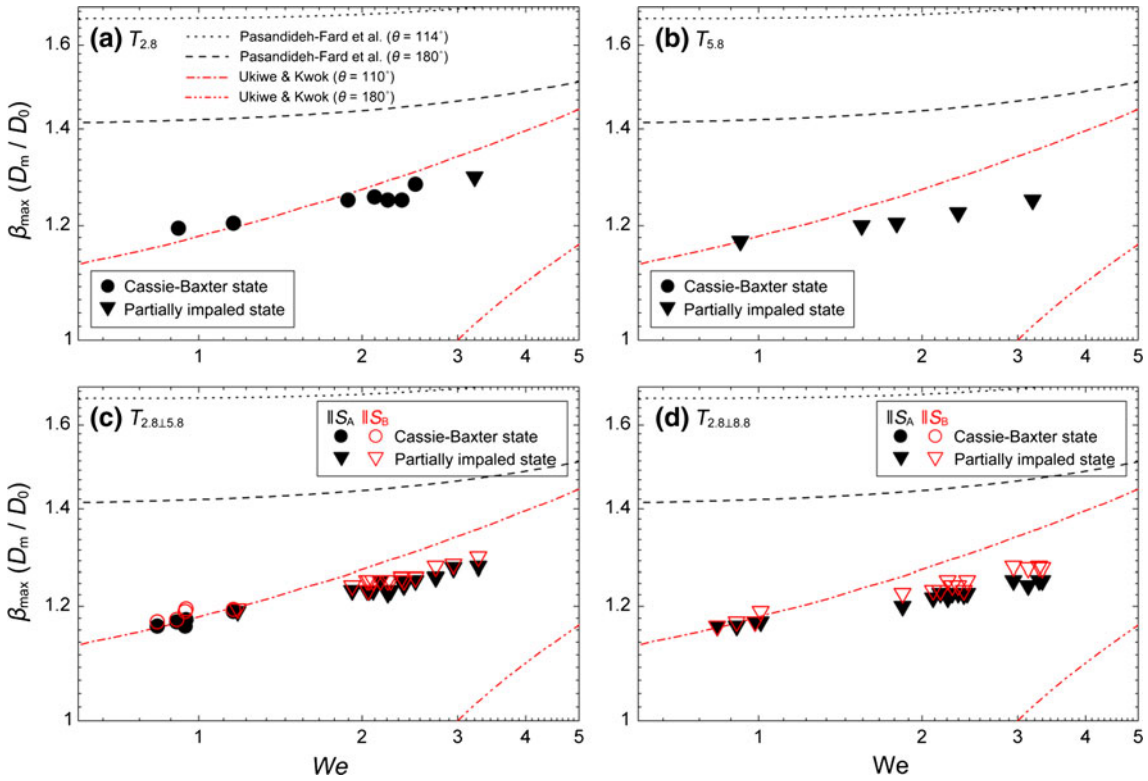

Fig. 11 Comparison of the prediction models with experimental values of the β_{max} in this study. The β_{max} on **a** $T_{2.8}$, **b** $T_{5.8}$, **c** $T_{2.8\perp5.8}$, and **d** $T_{2.8\perp8.8}$ are shown

pressure P_C even on the textured surfaces with anisotropic arrays of pillars. In addition, the Weber number *We* can be used to describe the transition between the bouncing and non-bouncing behaviors. Therefore, the wetting states and impact behaviors on the anisotropic arrays of pillars can be predicted and explained by the pressure range as well as the *We* of the impacting droplets.

To evaluate the anisotropic and directional wettability that arises from the anisotropic pattern of pillars, the maximum spreading factor (β_{max}) is measured and compared with the prediction models. The β_{max} of this study are smaller than those estimated in the capillary regime in which the β_{max} scales are $We^{1/4}$. The anisotropic and directional wettability is observed by measuring different β_{max} along the two orthogonal directions. The β_{max} along the direction of longer inter-pillar spacing (measured at $\|S_A$) always have smaller values than those along the direction of shorter inter-pillar spacing (measured at $\|S_B$). The difference in β_{max} along the two orthogonal directions increases as the length difference of the inter-pillar spacing ($\|S_A$ and $\|S_B$) increases. The overall values of the β_{max} for a given *We* are found to depend on the texture area fraction ϕ of the textured surfaces. Therefore, the wettability of the textured surface can be controlled by adjusting the length of each inter-pillar space because the ϕ depends on the inter-pillar spacing solely for a given pillar.

The measured β_{max} are compared with the prediction models based on the energy conservation condition. The model proposed by Ukiwe and Kwok (2005) demonstrates good agreement with our experimental results. Given that the model was established for a smooth surface condition, the relative error increases as the *We* increases so that the impalement transition occurs and the dissipation inside the texturing features increases.

Acknowledgments This work was supported by the National Research Foundation of Korea (NRF) grant funded by the Korea government (MSIP) (No. 2008–0061991).

References

Bartolo D, Bouamrirene F, Verneuil É, Buguin A, Silberzan P, Moulinet S (2006) Bouncing or sticky droplets: impalement transitions on superhydrophobic micropatterned surfaces. EPL 74(2):299–305

Bico J, Thiele U, Quere D (2002) Wetting of textured surfaces. Colloids Surf A 206(1–3):41–46

Bormashenko E, Pogreb R, Stein T, Whyman G, Erlich M, Musin A, Machavariani V, Aurbach D (2008) Characterization of rough surfaces with vibrated drops. Phys Chem Chem Phys 10(27): 4056–4061

Bormashenko E, Pogreb R, Whyman G, Balter S, Aurbach D (2012) Wetting transitions on post-built and porous reliefs. J Adhes Sci Technol 26(8–9):1169–1180

Cassie ABD, Baxter S (1944) Wettability of porous surfaces. Trans Faraday Soc 40:546–551

Clanet C, Béguin C, Richard D, Quéré D (2004) Maximal deformation of an impacting drop. J Fluid Mech 517:199–208

Deng T, Varanasi KK, Hsu M, Bhate N, Keimel C, Stein J, Blohm M (2009) Nonwetting of impinging droplets on textured surfaces. Appl Phys Lett 94(13):133109

Emami B, Tafreshi HV, Gad-el-Hak M, Tepper GC (2011) Predicting shape and stability of air-water interface on superhydrophobic surfaces with randomly distributed, dissimilar posts. Appl Phys Lett 98(20):203106

Engel OG (1955) Waterdrop collisions with solid surfaces. J Res Natl Bur Stand 54(5):281–298

Field JE (1999) ELSI conference: invited lecture—liquid impact: theory, experiment, applications. Wear 233:1–12

He B, Lee J, Patankar NA (2004) Contact angle hysteresis on rough hydrophobic surfaces. Colloids Surf A 248(1–3):101–104

Hyväluoma J, Timonen J (2009) Impact states and energy dissipation in bouncing and non-bouncing droplets. J Stat Mech: Theory Exp 06:P06010

Jung YC, Bhushan B (2008) Dynamic effects of bouncing water droplets on superhydrophobic surfaces. Langmuir 24(12): 6262–6269

Kannan R, Sivakumar D (2008) Impact of liquid drops on a rough surface comprising microgrooves. Exp Fluids 44(6):927–938

Kwon DH, Lee SJ (2012) Impact and wetting behaviors of impinging microdroplets on superhydrophobic textured surfaces. Appl Phys Lett 100(17):171601

Kwon H-M, Paxson AT, Varanasi KK, Patankar NA (2011) Rapid deceleration-driven wetting transition during pendant drop deposition on superhydrophobic surfaces. Phys Rev Lett 106(3):036102

Lafuma A, Quere D (2003) Superhydrophobic states. Nat Mater 2(7):457–460

Lee JB, Lee SH (2011) Dynamic wetting and spreading characteristics of a liquid droplet impinging on hydrophobic textured surfaces. Langmuir 27(11):6565–6573

Li X, Mao L, Ma X (2013) Dynamic behavior of water droplet impact on microtextured surfaces: the effect of geometrical parameters on anisotropic wetting and the maximum spreading diameter. Langmuir 29(4):1129–1138

Moulinet S, Bartolo D (2007) Life and death of a fakir droplet: impalement transitions on superhydrophobic surfaces. Eur Phys J E 24(3):251–260

Pasandideh-Fard M, Qiao YM, Chandra S, Mostaghimi J (1996) Capillary effects during droplet impact on a solid surface. Phys Fluids 8(3):650–659

Reyssat M, Pépin A, Marty F, Chen Y, Quéré D (2006) Bouncing transitions on microtextured materials. EPL 74(2):306–312

Reyssat M, Yeomans JM, Quéré D (2008) Impalement of fakir drops. EPL 81(2):26006

Schiaffino S, Sonin AA (1997) Molten droplet deposition and solidification at low weber numbers. Phys Fluids 9(11): 3172–3187

Sivakumar D, Katagiri K, Sato T, Nishiyama H (2005) Spreading behavior of an impacting drop on a structured rough surface. Phys Fluids 17(10):100608

Son Y, Kim C, Yang DH, Ahn DJ (2008) Spreading of an inkjet droplet on a solid surface with a controlled contact angle at low weber and Reynolds numbers. Langmuir 24(6):2900–2907

Ukiwe C, Kwok DY (2005) On the maximum spreading diameter of impacting droplets on well-prepared solid surfaces. Langmuir 21(2):666–673

Vaikuntanathan V, Kannan R, Sivakumar D (2010) Impact of water drops onto the junction of a hydrophobic texture and a hydrophilic smooth surface. Colloids Surf A 369(1–3):65–74

van Dam DB, Le Clerc C (2004) Experimental study of the impact of an ink-jet printed droplet on a solid substrate. Phys Fluids 16(9):3403–3414

Visser CW, Tagawa Y, Sun C, Lohse D (2012) Microdroplet impact at very high velocity. Soft Matter 8(41):10732–10737

Wenzel RN (1936) Resistance of solid surfaces to wetting by water. Ind Eng Chem 28(8):988–994

Xia DY, Brueck SRJ (2008) Strongly anisotropic wetting on one-dimensional nanopatterned surfaces. Nano Lett 8(9):2819–2824

Zhao Y, Lu QH, Li M, Li X (2007) Anisotropic wetting characteristics on submicrometer-scale periodic grooved surface. Langmuir 23(11):6212–6217

Zheng QS, Yu Y, Zhao ZH (2005) Effects of hydraulic pressure on the stability and transition of wetting modes of superhydrophobic surfaces. Langmuir 21(26):12207–12212